

## Saturn’s Evolutionary History and Seismology: Survival of Deep Stably Stratified Regions in Evolutionary Models of Saturn Consistent with Ring Seismology

YUBO SU ,<sup>1,2</sup> JANOSZ W. DEWBERRY ,<sup>3</sup> ROBERTO TEJADA AREVALO ,<sup>1</sup> ANKAN SUR ,<sup>1,4</sup> AND ADAM BURROWS ,<sup>1</sup>

<sup>1</sup> Department of Astrophysical Sciences, Princeton University, Princeton, NJ 08544, USA

<sup>2</sup> Canadian Institute for Theoretical Astrophysics, University of Toronto, 60 St George Street, Toronto, M5S 3H8 Ontario, Canada

<sup>3</sup> Department of Astronomy, University of Massachusetts Amherst, 710 N Pleasant St, Amherst, MA 01003, USA

<sup>4</sup> Department of Earth, Planetary, and Space Sciences, University of California Los Angeles, 595 Charles E Young Dr E, LA, CA 90095

### ABSTRACT

With recent advances in the modeling of the solar system giant planets, rapid progress has been made in understanding the remaining questions pertaining to their formation and evolution. However, this progress has largely neglected the significant constraints on the interior of Saturn’s structure imposed by the observed oscillation frequencies in its rings. Here, we study initial conditions for Saturn’s evolution that, after 4.56 Gyr of evolution, give rise to planetary structures admitting oscillation frequencies consistent with those observed via Saturn’s ring seismology. Restricting our attention to models without compact rocky cores, we achieve simultaneous good agreement with most observed properties of Saturn at the level of current evolutionary models and with key frequencies in the observed oscillation spectrum. Our preliminary work suggests that Saturn’s interior stably stratified region may be moderately less extended ( $\sim 0.4\text{--}0.5R_{\text{Sat}}$ ) than previously thought, which is important for reconciling the seismic constraints with evolutionary models. We also tentatively find that the deep helium gradients inferred by previous, static structural modelling of Saturn’s ring seismology may not be required to reproduce the observed seismology data.

*Keywords:* Planetary structure (1256) — Saturn (1426) — Planetary interior (1248)

### 1. INTRODUCTION

In traditional models of planet formation, gas giant planets are thought to form via a two-stage process, where the formation of a sufficiently massive rocky core is followed by runaway gas accretion (e.g. J. B. Pollack et al. 1996). Such a process is expected to form planets with a simple two-zone structure consisting of a compact rocky core and an extended gaseous envelope. The surprising evidence for extended composition gradients in the deep interiors of Jupiter and Saturn (e.g. S. M. Wahl et al. 2017; F. Debras & G. Chabrier 2019; B. Militzer et al. 2022; Y. Miguel et al. 2022; S. Howard et al. 2023; B. Militzer & W. B. Hubbard 2024) from the *Juno* (S. J. Bolton et al. 2017) and *Cassini* (L. Spilker 2019) missions has complicated this picture, posing new challenges for planet formation theory (see D. J. Stevenson 2020; R. Helled et al. 2022, for excellent reviews). Efforts to place such “fuzzy cores” in the context of the gas giants’ formation and evolution typically invoke 1) partial erosion and dilution of an initially compact core (T. Guillot et al. 2004; R. Moll et al. 2017; J. R. Fuentes

et al. 2025); 2) planetesimal collisions (S.-F. Liu et al. 2019; T. Meier et al. 2025); or 3) the conclusion that they are a natural consequence of the mass accretion process (C. W. Ormel et al. 2021; P. Bodenheimer et al. 2025). While such efforts are ongoing, it is clear that the inferred existence of fuzzy cores today place stringent constraints on the initial conditions and subsequent evolution of our giant planets’ structures (J. R. Fuentes et al. 2023; H. Knierim & R. Helled 2024; S. Markham & T. Guillot 2024; R. Tejada Arevalo et al. 2025; A. Sur et al. 2025c; H. Knierim et al. 2025).

Given the importance of accurately understanding giant planet fuzzy cores, observational constraints on their properties are at a premium. As such, the fortuitous coincidence that Saturn’s rings serve as an exquisite seismograph for its oscillation mode spectrum (D. J. Stevenson 1982; M. Hedman & P. Nicholson 2013; C. R. Mankovich 2020; R. G. French et al. 2021; V. M. Afigbo et al. 2025) provides invaluable insight into the extent and structure of Saturn’s deep interior (J. Fuller 2014; C. Mankovich et al. 2019; C. R. Mankovich & J. Fuller 2021). Note that, while there are tentative detections of

Jupiter's normal mode oscillations from ground-based interferometry (P. Gaulme et al. 2011; P. Gaulme et al. 2015) and from a detailed analysis of its gravitational field from *Juno* data (D. Durante et al. 2022), no data with the constraining power of the measurements made for Saturn are available at this time<sup>5</sup>. Nevertheless, it is clear that the incorporation of seismic constraints into giant planet evolution models are an important step towards understanding their deep interior structures.

In their seminal work, C. R. Mankovich & J. Fuller (2021) (hereafter MF21) found that the combination of Saturn's seismology and gravity data provided strong evidence for large-scale stable stratification extending from the core of the planet to  $\sim 0.6R_{\text{Sat}}$  at the present day, attributed to compositional gradients in both metal and helium. Subsequent work has provided additional inferences from the numerous oscillation modes identified (J. W. Dewberry et al. 2021, 2022; C. R. Mankovich et al. 2023), though these have largely advanced the characterization of Saturn's structure near its surface. In the opposite direction, modern evolutionary models find that the stably stratified interiors of giant planets become smaller over time via both thermodynamic (H. Knierim & R. Helled 2024; R. Tejada Arevalo et al. 2025; A. Sur et al. 2025c) and hydrodynamic (J. R. Fuentes et al. 2023; B. W. Hindman & J. R. Fuentes 2023; J. R. Fuentes et al. 2024; S. Zhang et al. 2025) mechanisms. The apparent conflicting demands of the present-day seismology and evolutionary perspectives pose a quantitative question: What initial conditions are required for a primordially stratified composition in Saturn to survive to the present day with a radial extent consistent with seismological constraints?

In this paper, we use the planet evolution code **APPLE** (A. Sur et al. 2024) to explore evolutionary histories for Saturn that are consistent with the seismological constraints from its rings. We seek two classes of answers to the question posed above. First, we aim to identify models that, similar to MF21, incorporate a primordial gradient in the fractional helium abundance (relative to hydrogen, i.e.,  $Y' \equiv Y/(1 - Z)$  where  $Y$  and  $Z$  are the absolute helium and metal mass fractions). Second, we explore models that begin with a uniform value of  $Y'$  set by the protosolar value, which has been the standard assumption for evolutionary models (e.g., D. J. Stevenson & E. E. Salpeter 1977; J. J. Fortney & W. B. Hubbard 2003; N. Nettelmann et al. 2015; R. Püstow et al. 2016;

<sup>5</sup> Note that the oscillations putatively detected by P. Gaulme et al. (2011) have surface radial velocities of  $\sim 50$  cm/s, while the typical surface velocities probed by ring seismology are  $\sim 0.05$  cm/s (J. Fuller 2014).

Quantity	Value	Reference
$R_{\text{eq}}$	$6.0268 \times 10^{10}$ cm	(1)
$T_{\text{eff}}$	96.67 K	(2)
$J_2 [\times 10^6]$	16290.573	(3)
$J_4 [\times 10^6]$	-935.314	(3)
$P_{\text{Sat}}$	38082 s	(4)
$\omega_{\text{W}84.64}/\Omega_{\text{dyn}}$	1.7153	(5)
$\omega_{\text{W}76.44}/\Omega_{\text{dyn}}$	1.9996	(5)
$A_{\text{W}84.64}/A_{\text{W}76.44}$	$3.80 \pm 0.40$	(6)

**Table 1.** Structural parameters (top) and seismological ones (bottom). Oscillation frequencies are given in the inertial frame. For reference, note that  $2\pi/(\Omega_{\text{dyn}}P_{\text{Sat}}) \simeq 0.38$ . References are: (1) P. K. Seidelmann et al. (2007), (2) L. Li et al. (2012), (3) L. Iess et al. (2019), (4) C. R. Mankovich et al. (2023), (5) R. G. French et al. (2019), (6) V. M. Afigbo et al. (2025).

C. R. Mankovich & J. J. Fortney 2020; A. Sur et al. 2025c). Through this exploration, we aim to isolate the constraints that motivate the proposed  $Y'$  gradient and quantify its effect in reproducing the observational constraints. We describe our methods in Section 2, present our models and their seismology in Section 3, discuss our results in the context of recent modeling efforts for Saturn in Section 4, and conclude in Section 5.

## 2. METHODS

In this section, we describe the methods we will use to evaluate our models. We first describe the observations that we seek to reproduce, and then we describe the numerical methods that we use to perform our planet modeling.

### 2.1. Observations

To evaluate our evolutionary models, we seek to match Saturn's observed equatorial radius  $R_{\text{eq}}$ , surface effective temperature  $T_{\text{eff}}$ , second  $J_2$  and fourth  $J_4$  gravitational zonal harmonics, and bulk rotation period  $P_{\text{Sat}}$ <sup>6</sup>. These values are provided in Table 1.

A few tens of oscillation frequencies have been identified in the rings (M. Hedman & P. Nicholson 2013; R. G. French et al. 2019; M. M. Hedman et al. 2019; R. G. French et al. 2021), and recent works have used

<sup>6</sup> While many other works attempt to fit for the surface  $Y$  and  $Z$  abundances (T. T. Koskinen & S. Guerlet 2018; T. Guillot et al. 2023), we defer this for future work: as we will discuss later, we do not include rocky cores in our analysis for technical reasons, so the  $Z$  distributions we obtain will likely differ significantly from better-fitting models that include compact, rocky cores. Indeed, the profiles we find have systematically large  $Z$  values at the surface, that will likely decrease in future work when compact rocky cores are included.

all of these frequencies to infer very tight constraints on the bulk rotation rate and near-surface rotation profile (C. Mankovich et al. 2019; C. R. Mankovich et al. 2023). However, most of these oscillation modes correspond to high angular number  $f$  modes that are largely insensitive to the deep interior structure of the planet. Instead, the four frequencies attributed to  $\ell = 2$  oscillation modes are the most constraining for the deep internal structure of Saturn. These are the Maxwell, W87.19, W84.64, and W76.44 frequencies (following the naming conventions of J. E. Colwell et al. 2009; R. G. French et al. 2019). Among these, the Maxwell and W87.19 frequencies are quite close to the inertial wave frequency range, which occurs when the wave frequency in the co-rotating frame of the planet  $\sigma$  satisfies  $|\sigma| < 2\Omega_{\text{Sat}}$ , where  $\Omega_{\text{Sat}} = 2\pi/P_{\text{Sat}}$  is Saturn's rotational angular frequency. Due to the singular nature of inertial wave oscillations in fluid bodies with a reflecting core (J. Goodman & C. Lackner 2009), the (inviscid) eigenvalue problem for their oscillation frequencies is ill-posed (though the initial value problem can be solved, J. C. B. Pa-paloizou & P. B. Ivanov 2010). As such, distinguishing the inertial modes requires both high spectral resolution and a source of wave damping, while these modes still depend sensitively on the physical and rotational structure of the planet. In the spirit of the exploratory nature of this work, we do not aim to resolve the spatially and spectrally dense inertial mode spectrum, and discard the Maxwell and W87.19 frequencies from our subsequent analysis.

The remaining W84.64 and, more importantly, the W76.44 frequencies furnish the strongest evidence for Saturn's deeply stratified core (J. Fuller 2014; C. R. Mankovich & J. Fuller 2021). The frequencies of these ring features are in Table 1, where they are given relative to Saturn's equatorial dynamical frequency  $\Omega_{\text{dyn}} \equiv \sqrt{GM_{\text{Sat}}/R_{\text{eq}}^3}$ , a characteristic frequency scale for gravitationally-restored  $f$  modes. Our primary objective in this section is to identify interior structures with sufficiently strong and extended stable stratification to reproduce the high-frequency W76.44 mode. Note that V. M. Afigbo et al. (2025) performed fits to the optical depth variations of the density rings in the waves to constrain the amplitudes of the planetary oscillations sourcing these variations, and their results are in Table 1. However, these amplitudes are proportional to the surface gravitational perturbations of their corresponding planetary mode, so they reflect the product of the mode amplitude and the mode eigenfunction's surface gravitational perturbation. Since calculating the oscillation modes of the planet yields only the latter quantity, the mode amplitude is unknowable without

further assumptions. One common assumption, which we will adopt here, is energy equipartition between these two modes (e.g., J. Fuller 2014; J. W. Dewberry et al. 2022). Under this assumption, the ratios of mode eigenfunctions' surface gravity perturbations can be directly compared to the observed ratio of optical depth variations. This assumption is of course unlikely to be exact, and so agreement with the observed amplitude ratio should be evaluated only at a qualitative level.

## 2.2. Numerics

We solve for Saturn's evolution using the planetary evolution code **APPLE** (A. Sur et al. 2024). Note that, in addition to the thermal, compositional, and structural evolution of the planet, **APPLE** solves for its deformation as well, using the fourth-order theory of figures (N. Nettelmann 2017), and includes an angle-averaged rotational contribution to the equation of hydrostatic equilibrium (A. Sur et al. 2024). The evolution of the planet's rotation rate is governed by the conservation of angular momentum. We adopt the hydrogen-helium equation of state from G. Chabrier & F. Debras (2021), and we treat the heavy elements using the AQUA equation of state (J. Haldemann et al. 2020), unless otherwise specified (see Section 3.3). The AQUA EOS contains an error in the entropy in S. Mazeved et al. (2019), and was corrected in S. Mazeved et al. (2021). This error does not affect the density and has now been shown to be inconsequential for the evolution of gas giants (A. Sur et al. 2025b) and even for Uranus and Neptune (R. Tejada Arevalo 2025). Given that this correction does not affect the density, it is not expected to affect the results of this paper. Finally, note that **APPLE** models semiconvective energy transport via the  $R_\rho$  parameterization. While this parameterization is often used in planetary evolution studies (e.g., C. Mankovich et al. 2016; A. Sur et al. 2024), it does not model physical semiconvection (e.g., J. Leconte & G. Chabrier 2012; T. S. Wood et al. 2013; A. Sur et al. 2025a). For clarity, we do not consider semiconvective energy transport in the models presented in this paper, so we set  $R_\rho = 1$ .

The atmospheric boundary conditions are adopted from Y.-X. Chen et al. (2023), and we follow A. Sur et al. (2025c) in interpolating these boundary conditions as functions of the helium and metal mass fractions at the base of the atmosphere. We model hydrogen-helium immiscibility (D. J. Stevenson & E. E. Salpeter 1977) using the second prescription described in A. Sur et al. (2024) ("scheme B," as also adopted in R. Helled et al. 2025) and use the miscibility curves of W. Lorenzen et al. (2009, 2011). Since improvements to the understanding of hydrogen-helium miscibility are ongoing (e.g. S.

Brygoo et al. 2021), we adopt the usual practice of using a temperature shift to the miscibility curves such that the resulting surface helium abundances match atmospheric observations (e.g., C. Mankovich et al. 2016; R. Tejada Arevalo et al. 2025; A. Sur et al. 2025c). Throughout this work, we adopt  $\Delta T = +410$  K. For the scale parameter  $\mathcal{H}_r$  over which helium demixes, we adopt  $2 \times 10^8$  cm. Note that, since the miscibility curves dynamically adjust to the pressure and temperature profiles of the planet, the resulting evolution is often stiff. To avoid this, we adopt a time lag prescription for the local critical immiscibility threshold  $Y'_m(P, T)$  (above which helium demixes), such that  $Y'_m$  approaches the instantaneous value derived from the miscibility curve on a timescale  $t_{Y_m, \text{lag}}$ . Since this is a purely numerical prescription, smaller values of  $t_{Y_m, \text{lag}}$  are preferred, and we adopt  $t_{Y_m, \text{lag}} = 5$  Myr throughout this work, one half our maximum timestep. We confirmed that different choices of  $t_{Y_m, \text{lag}} \gtrsim 1$  Myr do not affect the observed properties of the planet.

To calculate the oscillation frequencies of our Saturn models, we use the partial differential solver described in J. W. Dewberry et al. (2021, 2022); C. R. Mankovich et al. (2023). We refer the reader to these papers for further details on the numerical methods of this approach. In brief, the code takes in a smoothed<sup>7</sup> thermodynamic profile of the planet and its deformation via the shape functions from the theory of figures. Then it uses a 2D pseudo-spectral method to compute linearized oscillation modes, treating centrifugal flattening and the Coriolis force non-perturbatively. We use 120 Gauss-Lobatto collocation grid points in the (quasi-)radial direction, and project onto a spectral expansion in spherical harmonics truncated at degree  $\ell = 30$  (the projection integrals over planetary latitude are computed with a 257-point Gauss-Legendre quadrature). We find that increasing radial and spectral resolutions affects mode frequencies and surface gravitational perturbations negligibly (though see Section 3.1). The low resolution needed to resolve our modes is consistent with the fact that they are low-wavenumber oscillations with large frequency separations.

We perform searches for eigenvalues of the oscillation equations (corresponding to oscillation modes) in the range  $\omega \in [1.5, 2.4]\Omega_{\text{dyn}}$ . Additionally, we discard spectrally unresolved modes, where modes are designated spectrally resolved if the  $\ell = 30$  component of the mode eigenfunction is  $\lesssim 1\%$  of the maximum compo-

ment across all  $\ell$ . Mode eigenfunctions are normalized following the convention of F. A. Dahlen & J. Tromp (1999) (cf. J. W. Dewberry et al. 2021) such that the Lagrangian displacements are orthonormal. Then, mode energies in the co-rotating frame are given by  $\varepsilon_i = 2\sigma_i^2$  (A. K. Schenk et al. 2001), so we divide the mode amplitudes under normalization by  $\sigma_i/\sigma_{W84.64}$  to ensure energy equipartition (J. Fuller 2014; C. R. Mankovich & J. Fuller 2021). Finally, the modes are ordered by the  $\ell = 2$  component of their surface gravitational potential perturbation, denoted  $\Phi_{\ell=2, \text{surf}}$ , which are responsible for exciting the surface density fluctuations measured in the rings.

### 3. RESULTS

In this section, we aim to reproduce interior structure profiles as consistent as possible with the combined physical constraints on Saturn's bulk properties considered in previous works (e.g. A. Sur et al. 2025c,a) and those from seismology (M. Hedman & P. Nicholson 2013; C. R. Mankovich & J. Fuller 2021). We will consider four models in this section, and their attributes are summarized in Table 2.

#### 3.1. Comparison with Previous *APPLE* Models

Note that, as of this work, our oscillation frequency solver does not support a compact rocky core, which requires separate treatment due to the large density discontinuity at the interface. Such cores are present in the best-fitting evolutionary Saturn models obtained with *APPLE* (e.g. A. Sur et al. 2025c). As such, as a point of comparison for our later results, we first present the seismology results for a model similar to the best-fitting Saturn model from A. Sur et al. (2025c), but we remove the  $4M_{\oplus}$  core and distribute its metal content uniformly throughout the envelope. We also adjust the initial rotation rate such that the final rotation rate (under angular momentum conservation) remains consistent with the observed values. The resulting evolutionary track is shown in Fig. 1, and a comparison to the published model is shown in the light dashed lines in the two right panels. It can be seen that the removal of the core results in much larger magnitudes for  $J_2$  and  $J_4$ , a natural result of the lessened degree of central mass concentration in the planet.

Next, we show the surface gravitational potential perturbations as a function of the inertial-frame mode frequency for resolved modes in the searched frequency range in Fig. 2. We see that while a mode very near W84.64 appears (the  $f$  mode of the planet), no corresponding mode is found near the W76.44 frequency. Qualitatively, the W84.64 mode contains  $f$  mode characteristics (large near-surface perturbations), while a  $g$

<sup>7</sup> All fields are interpolated using a cubic spline except for the Brunt-Väisälä frequency, which is linearly interpolated to preserve non-negativity.

	Section	$Y'$ Gradient	Metal EOS	Fits Seismology?	Comments
Model 1	3.1	No	AQUA	No	Coreless ver. of S25
Model 2	3.2	Yes	AQUA	Yes	Resembling MF21
Model 3	3.3	No	AQUA	$\sim 5\%$	
Model 4	3.3	No	Postperovskite	$\sim 5\%$	

**Table 2.** Summary of models considered in Section 3 and their differences. S25 refers to A. Sur et al. (2025c).

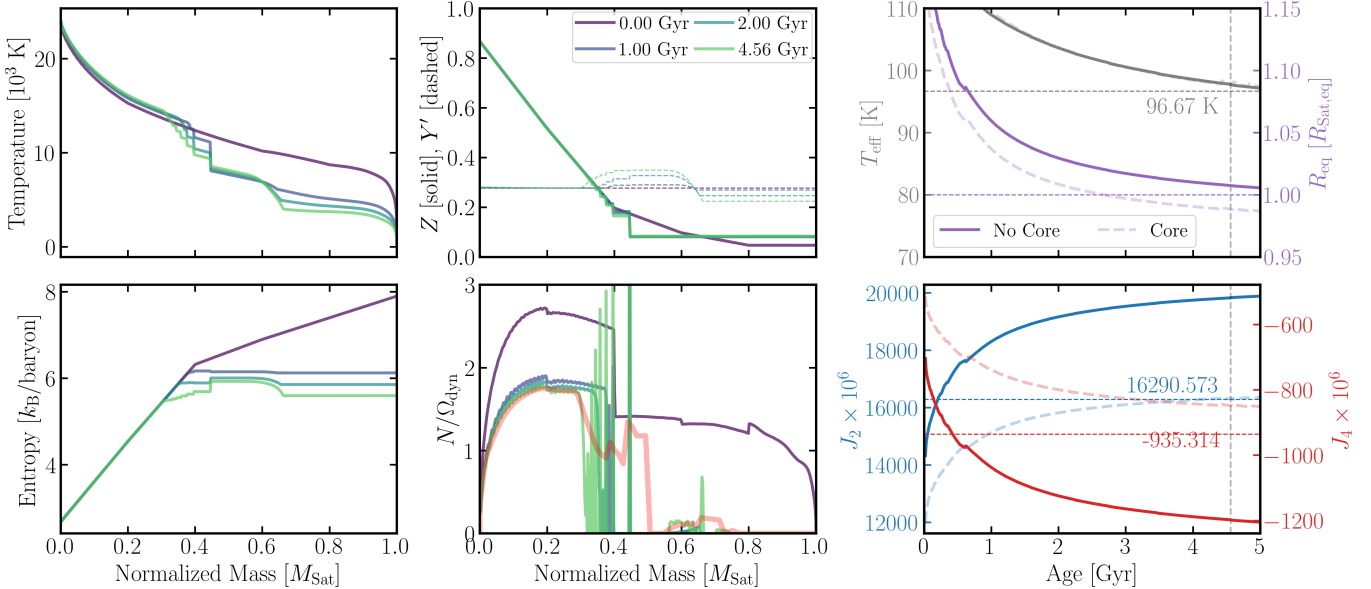


**Figure 1.** Evolution of the best-fitting Saturn model from A. Sur et al. (2025c) with its  $4M_{\oplus}$  compact core removed and redistributed uniformly throughout the envelope. The left four panels show the profiles of the internal temperature, entropy, heavy element mass fraction ( $Z$ ), fractional helium mass fraction ( $Y' \equiv Y/(1-Z)$ ), and the Brunt-Väisälä frequency  $N$  normalized to  $\Omega_{\text{dyn}} \equiv \sqrt{GM_{\text{Sat}}/R_{\text{eq}}^3}$  as functions of the normalized mass coordinate of Saturn at four times (legend in upper middle panel). The large variations in  $N$  are due to the discontinuities in the composition and thermal profiles of the planet (“stair steps”), which are commonly seen in 1D planetary evolution models (e.g. A. Vazan et al. 2018; R. Tejada Arevalo et al. 2025). The smoothed  $N$  profile that is used to compute oscillation modes is shown as the faint, thick red line. The right two panels show the temporal evolution of the effective temperature  $T_{\text{eff}}$ , the equatorial radius (in units of the measured equatorial radius of Saturn given in Table 1), and the gravitational zonal harmonics  $J_2$  and  $J_4$ . The vertical grey dashed line in the right two panels shows  $t = 4.56$  Gyr, the current age of Saturn. The final rotation rate is  $1.01 P_{\text{Sat}}$ . For comparison, the faint dashed lines in the right two panels show the evolution for the original model from A. Sur et al. (2025c) with a rocky core. We see that the presence of the rocky core reduces  $J_2$  and  $J_4$  by  $\sim 20\text{--}30\%$ , while the effect on  $T_{\text{eff}}$  and  $R_{\text{eq}}$  is much smaller.

mode (being mostly centrally confined) consistent with that found by C. R. Mankovich & J. Fuller (2021) is seen at a lower frequency than the W76.44 frequency. This suggests that the Brunt-Väisälä frequency in the deep interior of the planet is insufficiently large to source an oscillation frequency compatible with the W76.44 feature.

Uniquely in this model, we find that the many small discontinuities (in  $Z$ , temperature, and entropy) make the f-mode and the  $n = 1$  g-mode more difficult to resolve. Both appear to undergo avoided crossings with very short wavelength g-modes that do not contribute significantly to the  $\ell = 2$  gravitational perturbation, but which require spherical harmonic expansions extending

to degrees  $\ell \gtrsim 90$ . Additionally, increases in quasi-radial resolution (from 120 to 180) lead to frequency shifts on the order of  $\sim 0.01\%$  (versus  $\sim 0.0001\%$  for the other models). However, this error is still small, so our conclusions about the disagreement between this model and the ring seismology remains unchanged

### 3.2. With Helium Gradient

Next, in Fig. 3 we show a second model with a slightly shallower metal gradient, but with a linear gradient in  $Y'$  extending over the same range as that of  $Z$ , motivated by the suggestion in MF21. The entropy gradient is adjusted to compensate for a comparable temperature profile to that shown in Fig. 1. The resulting evolution is shown in Fig. 3, which contains a total of  $20M_{\oplus}$  of

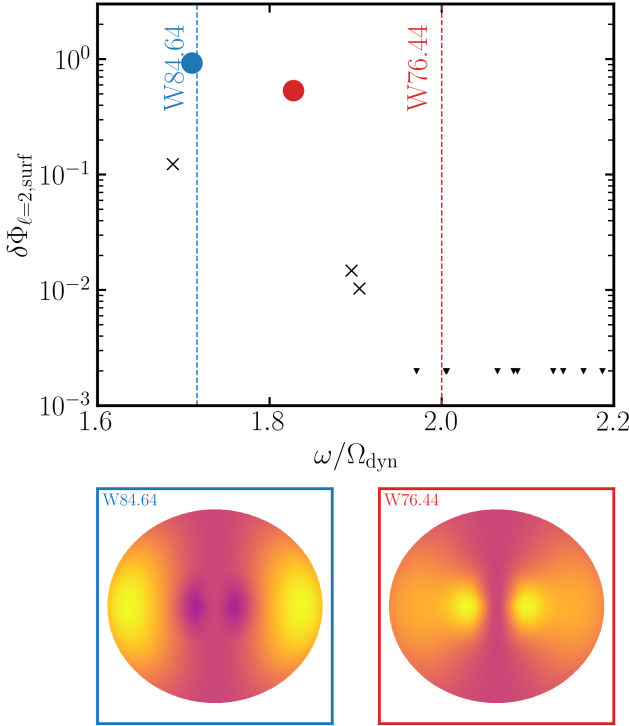


**Figure 2.** The top panel shows the surface gravitational potential perturbations for identified oscillation mode eigenfunctions for evolutionary model shown in Fig. 1 evaluated at  $t = 4.56$  Gyr, where the normalization is arbitrary but the relative amplitudes are correct under energy equipartition. The best candidate for the W84.64 frequency (vertical blue dashed line) is shown as the blue dot, the best candidate for the W76.44 frequency (vertical red dashed line) is shown as the red dot, and the other identified modes are shown as black crosses. It is clear that the identified  $g$  mode is too low in frequency to match the observed W76.44 frequency. Note that many modes are detected but have surface gravitational potential perturbations below the y-axis cutoff; we denote these with black triangles. The bottom two panels show color plots of the 2D gravitational potential perturbations ( $\delta\Phi$ ) of the two identified modes, color-coded and labeled.

heavy elements. Comparable agreement with observational constraints is seen, where the radius is too small and the gravity moments are too large. The absolute values of  $J_2$  and  $J_4$  are too large, but as seen in Fig. 1, the magnitude of this discrepancy is sufficiently small that it may be rectifiable by the addition of a compact core. Note that MF21 are able to obtain good agreement with  $J_2$  and  $J_4$  in their original work. In general, our models are hotter (less centrally dense) and have a higher surface helium abundance, resulting in a larger  $J_2$ , despite nearly identical radii and rotational periods.

On the other hand, this model is able to well-reproduce the seismology as can be seen in Fig. 4. By comparison of the Brunt-Väisälä profiles obtained in Fig. 1 and Fig. 3, we see that the larger values of  $N$  are sufficient to attain the W76.44 mode frequency. On the other hand, the outer extent of the stably stratified zone is  $\approx 0.5R_{\text{Sat}}$ , modestly smaller than the  $\sim 0.6R_{\text{Sat}}$  found by MF21 (and also corroborated by C. R. Mankovich et al. 2023). This difference is primarily mandated by the efficiency of fuzzy core erosion in our evolutionary models: As the surface cools, the convective exterior of the planet grows (see H. Knierim & R. Helled 2024 for an excellent theoretical model describing the process). Thus, the fact that Saturn must cool for 4.56 Gyr imposes an effective upper limit on the maximum extent of the stably stratified interior region. We recall that the mode responsible for sourcing the W76.44 frequency is attributed to an avoided crossing between the surface  $\ell = 2$   $f$  mode and an interior  $n = 1$ ,  $\ell = 2$   $g$  mode (C. R. Mankovich & J. Fuller 2021). An upshot is that the combination of a smaller cavity and a larger  $N$  inside the cavity yields a comparable  $g$  mode frequency. Even a reduced radial extent of the cavity still produces a sufficiently strong avoided crossing to manifest a large surface perturbation, comparable to that found by MF21.

We briefly comment that Fig. 4 shows an additional mode near the W76.44 that corresponds to a rosette mode (M. Takata & H. Saio 2013; J. W. Dewberry et al. 2021) that undergoes an avoided crossing with the identified  $g$  mode. The non-detection of a doublet at the W76.44 frequency in ring wave observations suggests that this exact model should be modestly disfavored. However, given the strong sensitivity of rosette modes to small features in the planet's structure, it is difficult to draw concrete conclusions on whether small modifications to the planet's structure will remove this doublet or whether this class of models should be disfavored by the data. Empirically, we find that rosette modes near the W76.44 frequency appear in many of our models, though their relative gravitational perturbations can easily be reduced with small modifications to the planet's structure.

### 3.3. Uniform Helium Concentration

While the model shown in Fig. 3 yields a mostly satisfactory fit by evolutionary standards, it has one point of discomfort: why should there be a primordial gradient in the helium composition  $Y'$ ? Naively,  $Y'$  should be set by the protosolar composition. With this in mind, we study models with uniform initial  $Y'$  profiles. As seen from the results of Section 3.2, a large value of the Brunt-Väisälä frequency  $N$  in the deep interior is required to admit a

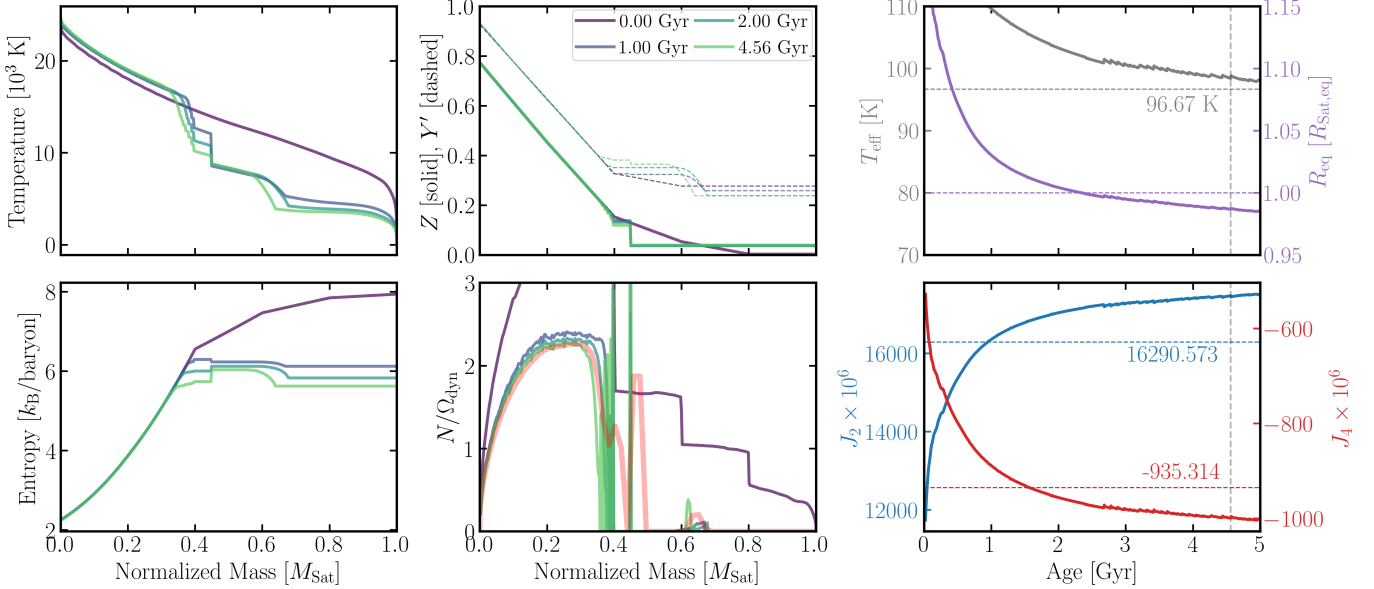


**Figure 3.** Same as Fig. 1 but for a model with a deep linear gradient in  $Y' \equiv Y/(1 - Z)$  (similar to C. R. Mankovich & J. Fuller 2021) and similar  $Z$  and entropy profiles. An elevated Brunt-Väisälä frequency compared to the model shown in Fig. 1 can be seen due to the additional composition stratification, resulting in better agreement with the ring seismology constraints (see Fig. 4). Similar to Fig. 1, the  $J_2$  and  $J_4$  values are elevated compared to their observed values. The final spin period is  $0.995 P_{\text{Sat}}$ .

$g$  mode with a sufficiently high frequency to match the W76.44 mode. Since there is a smaller  $Y$  gradient, and both  $Y$  and  $Z$  gradients contribute to the value of  $N$  (cf. R. Tejada Arevalo et al. 2024), a steeper  $Z$  gradient is required. As such, we consider initial  $Z$  profiles moderately steeper than those considered in Section 3.2. With some small manual adjustments of the initial  $Z$  and entropy profiles, we arrive at the model shown in Fig. 5, which contains a total of  $22M_{\oplus}$  of heavy elements. Note that the Brunt-Väisälä profile is somewhat larger and less extended.

The corresponding seismology can be seen in Fig. 6. The agreement is excellent and is marginally better than the model with a  $Y'$  gradient studied above (Fig. 4). Note also that while the radius of the inner stable region is only  $\approx 0.43R_{\text{Sat}}$ , the surface gravitational perturbation is not significantly affected. This suggests that the theoretical predictions for the  $m = 2$  ring frequencies are not exceptionally sensitive to  $R_{\text{stab}}$  (though this may no longer be the case when including the observed  $m = 3$  ring waves; J. Fuller 2014; J. W. Dewberry et al. 2021).

To explore the effect of uncertainties in the heavy element equation of state on the inferred structures and observables, we also consider models where the metals are treated using a postperovskite equation of state ( $\text{MgSiO}_3$ ; A. Keane 1954; F. D. Stacey & P. M. Davis 2004; J. Zhang & L. A. Rogers 2022). An example model retaining satisfactory agreement with the seismology is

shown in Fig. 7, which contains a total of  $19M_{\oplus}$  of heavy elements. This model has inner stable region extent  $\approx 0.44R_{\text{Sat}}$ . Note that the overall heavy element mass fraction ( $Z$ ) in the deep interior is lower. This is because postperovskite is denser at similar temperatures than water, so when using similar temperature profiles, stronger stratification and larger Brunt-Väisälä frequencies are produced. As such, when the target Brunt-Väisälä profile is held fixed, a shallower  $Z$  gradient arises for postperovskite than for water. The agreement with the known seismological frequencies remains quite good, as can be seen in Fig. 7. Note that now a doublet appears near the  $f$  mode, due to an avoided crossing with a rosette mode in the deep core. Again, similarly to the model shown in Fig. 4, we note that this model should strictly be disfavored due to this doublet, but that small changes to the interior structure can easily detune the avoided crossing and remove the doublet.

#### 4. DISCUSSION

We have shown that good simultaneous agreement with most of the listed properties in Table 1 can be achieved both with a primordial  $Y'$  gradient (Section 3.2) and without (Section 3.3), with the caveat of moderate discrepancies in reproducing the gravitational harmonics  $J_2$  and  $J_4$ . By comparison to our previous modeling efforts, we suggest that these discrepancies are due to the absence of a rocky core in the models considered here. We anticipate that similar structures to

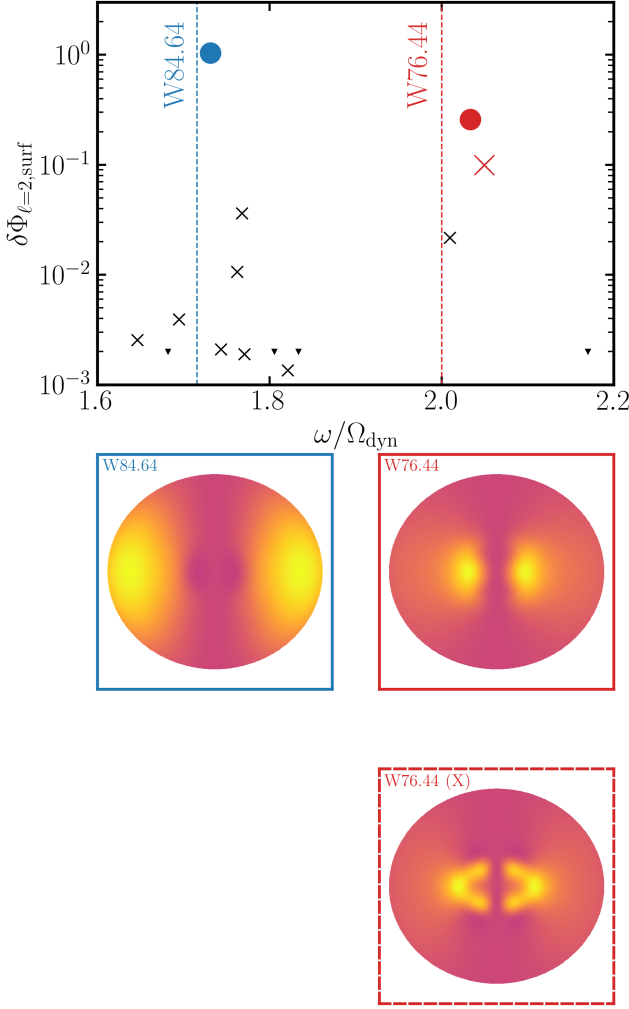


**Figure 4.** Same as Fig. 2, but for the model shown in Fig. 3 containing a  $Y'$  gradient. Both the W84.64 and W76.44 frequencies are well-matched. The eigenfunctions shown in the bottom row do not show rosette-like features, and we find that the W84.64 mode appears  $f$ -mode-like, while the W76.44 mode appears  $g$ -mode-like, in agreement with previous work (MF21). The mode with which the  $g$  mode near the W76.44 frequency undergoes an avoided crossing is shown in the third row, with the dashed borders; its corresponding mode frequency and amplitude are shown with the colored cross in the top panel.

those presented here can be found that both have rocky cores and fit all of Saturn's observables, though future numerical work is necessary to confirm this. Below, we discuss our results in the context of previous work in the literature.

We begin with an in-depth comparison between previous static structural modeling of Saturn incorporating ring seismology (MF21, J. W. Dewberry et al. 2021, 2022; C. R. Mankovich et al. 2023) and our current work. Both their models and ours yield comparable

estimates for Saturn's rotation rate, radius, and seismology. However, the stably stratified cores in their models are markedly more extended than ours (with an outermost radius  $R_{\text{stab}} \sim 0.6R_{\text{Sat}}$ ), they obtain good fits to the gravitational moments  $J_2$  and  $J_4$  of Saturn, and they impose a primordial  $Y'$  gradient. By contrast, our models have more compact stably stratified regions ( $R_{\text{stab}} \approx 0.4\text{--}0.5R_{\text{Sat}}$ ), generally overpredict the  $J_2$  and  $J_4$  values, and do not require a primordial  $Y'$  gradient.

First, we remark that the difference in stable region extent is largely driven by evolutionary constraints. In our models, the combined constraints of Saturn's present-day radius and that enough metals be present in the deep interior to source a large Brunt-Väisälä frequency place a lower bound on the initial entropies and temperatures of Saturn—if the planet is too cool, it must either have a small present-day radius or low concentrations of heavy elements. Then, with such a minimum luminosity imposed,  $R_{\text{stab}}$  must erode by some corresponding minimum amount. While this constraint can be relaxed somewhat by decreasing the total metal content and allowing a primordial  $Y'$  gradient to contribute to the Brunt-Väisälä frequency, the physical motivation for such an initial condition is unclear.

Second, we remark that these smaller  $R_{\text{stab}}$  values contribute significantly to our overestimated  $J_2$  and  $J_4$  values. We find that in evolutionary models where the present-day  $R_{\text{stab}}$  is larger, we successfully reproduce the observed  $J_2$  and  $J_4$  values even in absence of a rocky core. However, for reasons discussed above, such evolutionary models fail to fit either the radius or seismology results. Motivated by our previous Saturn models that required a compact rocky core (as shown in Fig. 1, A. Sur et al. 2025c), we suggest that the addition of a rocky core to evolutionary models will reduce  $J_2$  and  $J_4$  (by  $\sim 25\%$ ) while preserving simultaneous fits of all observed properties of Saturn. The modest radial extent of these cores ( $\sim 0.13R_{\text{Sat}}$ ) seems to indicate that their impact on our seismological results will be smaller than on  $J_2$  and  $J_4$ . For instance, J. Fuller et al. (2014) find that a solid core with extent  $\sim 0.2R_{\text{Sat}}$  has small effects on the  $f$  mode frequencies.

Third, our models with and without primordial  $Y'$  gradients yield comparable fits to the seismological results (see Figs. 4 and 6). Furthermore, comparison of models using AQUA and post-perovskite as the heavy element equation of state (Section 3.3) exhibit significantly different compositional profiles, yet mostly similar observable properties. We conclude that there appears to be some inherent degeneracy between the heavy element composition and its concentration/distribution in Saturn, though there may

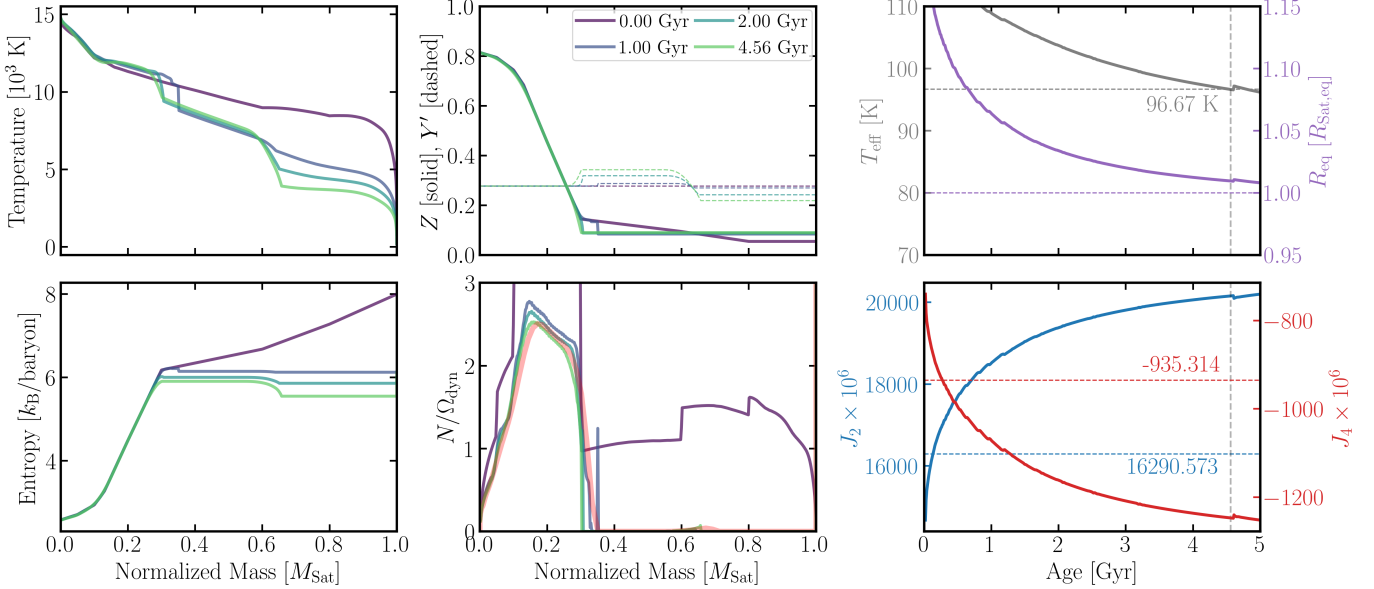


**Figure 5.** Similar to Fig. 1 but for a model with initially uniform  $Y' \equiv Y/(1 - Z)$  and a steeper  $Z$  profile. The final spin period is  $0.994P_{\text{Sat}}$ . Comparable agreement with observational constraints is seen in all panels.

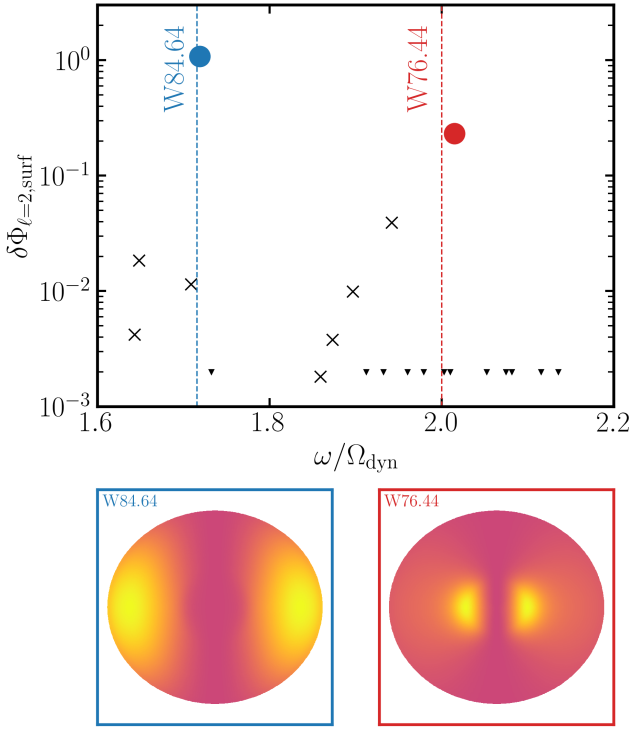


**Figure 6.** Seismology for a model corresponding to Fig. 5. Excellent agreement is observed.

be prospects for reducing the degeneracy in higher-precision future work.

Finally, we observe that MF21 considered only adiabatic (marginally Schwarzschild unstable) temperature/entropy gradients, with the motivation that efficient semi-convection likely smooths out superadiabatic

stratification on short timescales. The initial entropy profiles we explore are created without particular regard for the adiabaticity of the stratification, though we verify *a posteriori* that our profiles are approximately adiabatic as well. Our results suggest that future work exploring Saturn's heavy element composition (e.g., mixtures of water, rock, iron), in conjunction with a rocky core, will likely yield sufficiently good agreement with observations that the primordial helium-hydrogen ratio can be taken to be uniformly protosolar.

Separately, we have not considered semi-convective energy and composition transport in this work. The inclusion of semi-convection likely has marginal effects in the models we study, where the interiors are approximately marginally Schwarzschild unstable and the surface envelope region is fully convective. However, future detailed numerical work will be required to explore the effect of semi-convection. Note that, if the stably stratified region is semi-convective, it may give rise to magnetic dynamos (P. Pržina et al. 2025) that help reproduce the observed axisymmetry of Saturn's magnetic field (D. J. Stevenson 1982; S. Stanley 2010; C. Yan & S. Stanley 2021).

It has been suggested that a helium compositional gradient due to immiscibility may affect the seismic oscillations considered here, in addition to a primordial composition gradient. In our models, we find that there is generally no effect on the  $\ell = 2$  modes, and an analytic argument justifying this lack of an effect is given in Appendix A.

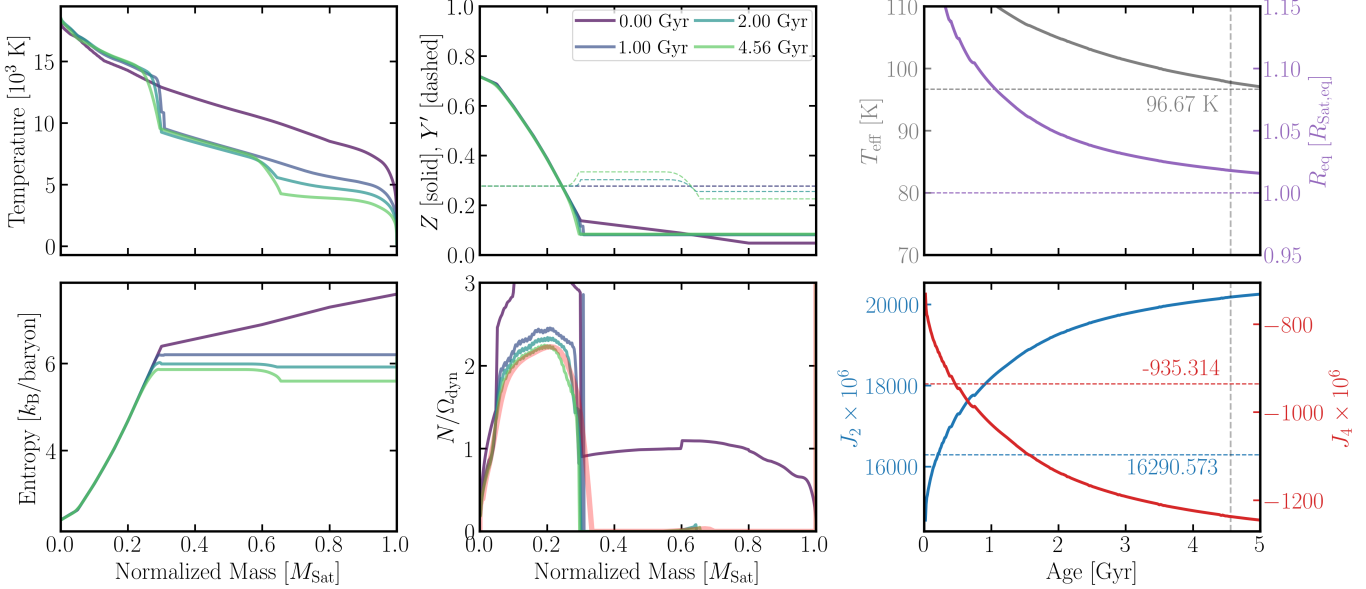


**Figure 7.** Similar to Fig. 5 but for different profiles adapted for a postperovskite heavy element equation of state (J. Zhang & L. A. Rogers 2022). While the planetary structure is quite different, the resulting agreement with observables is quite similar. The final rotation period is  $0.989 P_{\text{Sat}}$ .

### 5. SUMMARY

A significant challenge to the modern understanding of giant planet formation is the discovery of extended stably stratified “fuzzy cores.” The strongest constraints on the extent of these fuzzy cores are obtained by seismological inference of features in the rings of Saturn (C. R. Mankovich & J. Fuller 2021). The presence of these extended fuzzy cores poses a challenge for planetary evolution models, which find that the extent of fuzzy cores should generally decrease as the planet evolves, for a mixture of thermodynamic and hydrodynamic reasons.

In this work, we have used giant planet evolutionary models to understand the balance between these two competing demands. Our work shows that these two effects can be reconciled: a sufficiently extended stably stratified core consistent with constraints from ring seismology can survive to the present day. Our models generally require steeper stratification than evolutionary models in the literature today, but suggest less extended fuzzy cores compared to static model inferences from ring seismology (C. R. Mankovich & J. Fuller 2021).

Our combined approach and results illustrate the importance of ring seismology towards constraining planetary interior evolution. Furthermore, by comparing our models that exhibit good fits to the observed properties of Saturn, we conclude that the possible presence of a compact rocky core are the most promising avenues for improved fits to Saturn’s present-day structure. We defer exploration of these effects to future work.

### ACKNOWLEDGEMENTS

YS acknowledges support by the Lyman Spitzer Jr. Postdoctoral Fellowship at Princeton University and by the Natural Sciences and Engineering Research Council of Canada (NSERC) [funding reference CITA 490888-16]. Partial funding for this research was provided by the Center for Matter at Atomic Pressures (CMAP), a National Science Foundation (NSF) Physics Frontier Center, under Award PHY-2020249. Any opinions, findings, conclusions or recommendations expressed in this material are those of the author(s) and do not necessarily reflect those of the National Science Foundation.

### REFERENCES

Afigbo, V. M., Hedman, M. M., Nicholson, P. D., et al. 2025, Journal of Geophysical Research (Planets), 130, e2024JE008710, doi: [10.1029/2024JE008710](https://doi.org/10.1029/2024JE008710)

Bodenheimer, P., Stevenson, D. J., Lissauer, J. J., & D’Angelo, G. 2025, PSJ, 6, 143, doi: [10.3847/PSJ/add0b0](https://doi.org/10.3847/PSJ/add0b0)

Bolton, S. J., Adriani, A., Adumitroaie, V., et al. 2017, Science, 356, 821

Bryggo, S., Loubeyre, P., Millot, M., et al. 2021, Nature, 593, 517, doi: [10.1038/s41586-021-03516-0](https://doi.org/10.1038/s41586-021-03516-0)

Chabrier, G., & Debras, F. 2021, The Astrophysical Journal, 917, 4

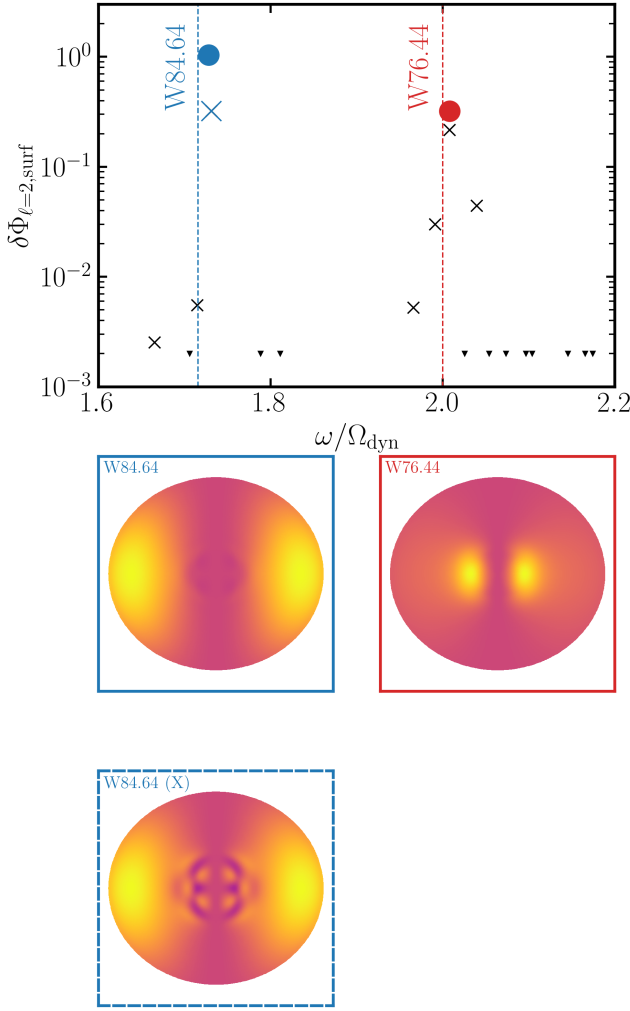


**Figure 8.** Seismology for model corresponding to Fig. 7. Another avoided crossing is highlighted, this time with the  $f$  mode, in the third row.

Chen, Y.-X., Burrows, A., Sur, A., & Arevalo, R. T. 2023, *ApJ*, 957, 36, doi: [10.3847/1538-4357/acf456](https://doi.org/10.3847/1538-4357/acf456)

Colwell, J. E., Nicholson, P. D., Tiscareno, M. S., et al. 2009, in *Saturn from Cassini-Huygens*, ed. M. K. Dougherty, L. W. Esposito, & S. M. Krimigis, 375, doi: [10.1007/978-1-4020-9217-6\\_13](https://doi.org/10.1007/978-1-4020-9217-6_13)

Dahlen, F. A., & Tromp, J. 1999, *Theoretical Global Seismology* (Princeton University Press)

Debras, F., & Chabrier, G. 2019, *The Astrophysical Journal*, 872, 100

Dewberry, J. W., Mankovich, C. R., & Fuller, J. 2022, *MNRAS*, 516, 358, doi: [10.1093/mnras/stac1957](https://doi.org/10.1093/mnras/stac1957)

Dewberry, J. W., Mankovich, C. R., Fuller, J., Lai, D., & Xu, W. 2021, *PSJ*, 2, 198, doi: [10.3847/PSJ/ac0e2a](https://doi.org/10.3847/PSJ/ac0e2a)

Durante, D., Guillot, T., Iess, L., et al. 2022, *Nature communications*, 13, 4632

Fortney, J. J., & Hubbard, W. B. 2003, *Icarus*, 164, 228, doi: [10.1016/S0019-1035\(03\)00130-1](https://doi.org/10.1016/S0019-1035(03)00130-1)

French, R. G., Bridges, B., Hedman, M. M., et al. 2021, *Icarus*, 370, 114660, doi: [10.1016/j.icarus.2021.114660](https://doi.org/10.1016/j.icarus.2021.114660)

French, R. G., McGhee-French, C. A., Nicholson, P. D., & Hedman, M. M. 2019, *Icarus*, 319, 599, doi: [10.1016/j.icarus.2018.10.013](https://doi.org/10.1016/j.icarus.2018.10.013)

Fuentes, J. R., Anders, E. H., Cumming, A., & Hindman, B. W. 2023, *ApJL*, 950, L4, doi: [10.3847/2041-8213/acd774](https://doi.org/10.3847/2041-8213/acd774)

Fuentes, J. R., Hindman, B. W., Fraser, A. E., & Anders, E. H. 2024, *ApJL*, 975, L1, doi: [10.3847/2041-8213/ad84dc](https://doi.org/10.3847/2041-8213/ad84dc)

Fuentes, J. R., Mankovich, C. R., & Sur, A. 2025, *ApJL*, 988, L49, doi: [10.3847/2041-8213/adef0a](https://doi.org/10.3847/2041-8213/adef0a)

Fuller, J. 2014, *Icarus*, 242, 283

Fuller, J., Lai, D., & Storch, N. I. 2014, *Icarus*, 231, 34, doi: [10.1016/j.icarus.2013.11.022](https://doi.org/10.1016/j.icarus.2013.11.022)

Garaud, P. 2018, *Annu. Rev. Fluid Mech.*, 50, 275, doi: [10.1146/annurev-fluid-122316](https://doi.org/10.1146/annurev-fluid-122316)

Gaulme, P., Mosser, B., Schmider, F. X., & Guillot, T. 2015, in *Extraterrestrial Seismology*, ed. V. Tong & R. Garcí (Cambridge University Press), 189–202, doi: [10.1017/CBO9781107300668.017](https://doi.org/10.1017/CBO9781107300668.017)

Gaulme, P., Schmider, F.-X., Gay, J., Guillot, T., & Jacob, C. 2011, *Astronomy & Astrophysics*, 531, A104

Goodman, J., & Lackner, C. 2009, *ApJ*, 696, 2054, doi: [10.1088/0004-637X/696/2/2054](https://doi.org/10.1088/0004-637X/696/2/2054)

Guillot, T., Fletcher, L. N., Helled, R., et al. 2023, in *Astronomical Society of the Pacific Conference Series*, Vol. 534, *Protostars and Planets VII*, ed. S. Inutsuka, Y. Aikawa, T. Muto, K. Tomida, & M. Tamura, 947

Guillot, T., Stevenson, D. J., Hubbard, W. B., & Saumon, D. 2004, in *Jupiter. The Planet, Satellites and Magnetosphere*, ed. F. Bagenal, T. E. Dowling, & W. B. McKinnon, Vol. 1 (Cambridge Univ. Press Cambridge, U. K.), 35–57

Haldemann, J., Alibert, Y., Mordasini, C., & Benz, W. 2020, *A&A*, 643, A105, doi: [10.1051/0004-6361/202038367](https://doi.org/10.1051/0004-6361/202038367)

Hedman, M., & Nicholson, P. 2013, *The Astronomical Journal*, 146, 12

Hedman, M. M., Nicholson, P. D., & French, R. G. 2019, *AJ*, 157, 18, doi: [10.3847/1538-3881/aaf0a6](https://doi.org/10.3847/1538-3881/aaf0a6)

Helled, R., Müller, S., & Knierim, H. 2025, *A&A*, 704, A253, doi: [10.1051/0004-6361/202556537](https://doi.org/10.1051/0004-6361/202556537)

Helled, R., Stevenson, D. J., Lunine, J. I., et al. 2022, *Icarus*, 114937

Hindman, B. W., & Fuentes, J. R. 2023, *ApJL*, 957, L23, doi: [10.3847/2041-8213/ad0642](https://doi.org/10.3847/2041-8213/ad0642)

Howard, S., Guillot, T., Bazot, M., et al. 2023, arXiv e-prints, arXiv:2302.09082

Iess, L., Militzer, B., Kaspi, Y., et al. 2019, *Science*, 364, eaat2965

Keane, A. 1954, *Australian Journal of Physics*, 7, 322, doi: [10.1071/PH540322](https://doi.org/10.1071/PH540322)

Knierim, H., Batygin, K., Helled, R., Morf, L., & Adams, F. C. 2025, arXiv e-prints, arXiv:2512.03961, doi: [10.48550/arXiv.2512.03961](https://doi.org/10.48550/arXiv.2512.03961)

Knierim, H., & Helled, R. 2024, *ApJ*, 977, 227, doi: [10.3847/1538-4357/ad8dd0](https://doi.org/10.3847/1538-4357/ad8dd0)

Koskinen, T. T., & Guerlet, S. 2018, *Icarus*, 307, 161, doi: [10.1016/j.icarus.2018.02.020](https://doi.org/10.1016/j.icarus.2018.02.020)

Leconte, J., & Chabrier, G. 2012, *A&A*, 540, 20, doi: [10.1051/0004-6361/201117595](https://doi.org/10.1051/0004-6361/201117595)

Leconte, J., & Chabrier, G. 2013, *Nature Geoscience*, doi: [10.1038/NGEO1791](https://doi.org/10.1038/NGEO1791)

Ledoux, P. 1947, *ApJ*, 105

Li, L., Baines, K. H., Smith, M. A., et al. 2012, *Journal of Geophysical Research (Planets)*, 117, E11002, doi: [10.1029/2012JE004191](https://doi.org/10.1029/2012JE004191)

Liu, S.-F., Hori, Y., Müller, S., et al. 2019, *Natur*, 572, 355, doi: [10.1038/s41586-019-1470-2](https://doi.org/10.1038/s41586-019-1470-2)

Lorenzen, W., Holst, B., & Redmer, R. 2009, *PhRvL*, 102, 115701, doi: [10.1103/PhysRevLett.102.115701](https://doi.org/10.1103/PhysRevLett.102.115701)

Lorenzen, W., Holst, B., & Redmer, R. 2011, *PhRvB*, 84, 235109, doi: [10.1103/PhysRevB.84.235109](https://doi.org/10.1103/PhysRevB.84.235109)

Mankovich, C., Fortney, J. J., & Moore, K. L. 2016, *ApJ*, 832, 113, doi: [10.3847/0004-637X/832/2/113](https://doi.org/10.3847/0004-637X/832/2/113)

Mankovich, C., Marley, M. S., Fortney, J. J., & Movshovitz, N. 2019, *The Astrophysical Journal*, 871, 1

Mankovich, C. R. 2020, *AGU Advances*, 1, 1, doi: [10.1029/2019av000142](https://doi.org/10.1029/2019av000142)

Mankovich, C. R., Dewberry, J. W., & Fuller, J. 2023, *PSJ*, 4, 59, doi: [10.3847/PSJ/acc253](https://doi.org/10.3847/PSJ/acc253)

Mankovich, C. R., & Fortney, J. J. 2020, *ApJ*, 889, 51, doi: [10.3847/1538-4357/ab6210](https://doi.org/10.3847/1538-4357/ab6210)

Mankovich, C. R., & Fuller, J. 2021, *Nature Astronomy*, 5, 1103

Markham, S., & Guillot, T. 2024, *PSJ*, 5, 269, doi: [10.3847/PSJ/ad8449](https://doi.org/10.3847/PSJ/ad8449)

Mazevet, S., Licari, A., Chabrier, G., & Potekhin, A. Y. 2019, *Astronomy and Astrophysics*, 621, 1, doi: [10.1051/0004-6361/201833963](https://doi.org/10.1051/0004-6361/201833963)

Mazevet, S., Licari, A., Chabrier, G., & Potekhin, A. Y. 2021, *Astronomy and Astrophysics*, 621, 1, doi: [10.1051/0004-6361/201833963](https://doi.org/10.1051/0004-6361/201833963)

Meier, T., Reinhardt, C., Shibata, S., et al. 2025, arXiv e-prints, arXiv:2503.23997, doi: [10.48550/arXiv.2503.23997](https://doi.org/10.48550/arXiv.2503.23997)

Miguel, Y., Bazot, M., Guillot, T., et al. 2022, *A&A*, 662, A18, doi: [10.1051/0004-6361/202243207](https://doi.org/10.1051/0004-6361/202243207)

Militzer, B., & Hubbard, W. B. 2024, *Icarus*, 411, 115955, doi: [10.1016/j.icarus.2024.115955](https://doi.org/10.1016/j.icarus.2024.115955)

Militzer, B., Hubbard, W. B., Wahl, S., et al. 2022, *The planetary science journal*, 3, 185

Moll, R., Garaud, P., Mankovich, C., & Fortney, J. J. 2017, *ApJ*, 849, 24, doi: [10.3847/1538-4357/aa8d74](https://doi.org/10.3847/1538-4357/aa8d74)

Nettelmann, N. 2017, *Astronomy and Astrophysics*, 606, 1, doi: [10.1051/0004-6361/201731550](https://doi.org/10.1051/0004-6361/201731550)

Nettelmann, N., Fortney, J. J., Moore, K., & Mankovich, C. 2015, *MNRAS*, 447, 3422, doi: [10.1093/mnras/stu2634](https://doi.org/10.1093/mnras/stu2634)

Ormel, C. W., Vazan, A., & Brouwers, M. G. 2021, *A&A*, 647, A175, doi: [10.1051/0004-6361/202039706](https://doi.org/10.1051/0004-6361/202039706)

Papaloizou, J. C. B., & Ivanov, P. B. 2010, *MNRAS*, 407, 1631, doi: [10.1111/j.1365-2966.2010.17011.x](https://doi.org/10.1111/j.1365-2966.2010.17011.x)

Pollack, J. B., Hubickyj, O., Bodenheimer, P., et al. 1996, *Icarus*, 124, 62, doi: [10.1006/icar.1996.0190](https://doi.org/10.1006/icar.1996.0190)

Pružina, P., Cébron, D., & Schaeffer, N. 2025, *A&A*, 703, A135, doi: [10.1051/0004-6361/202556134](https://doi.org/10.1051/0004-6361/202556134)

Püstow, R., Nettelmann, N., Lorenzen, W., & Redmer, R. 2016, *Icarus*, 267, 323, doi: [10.1016/j.icarus.2015.12.009](https://doi.org/10.1016/j.icarus.2015.12.009)

Schenk, A. K., Arras, P., Flanagan, É. É., Teukolsky, S. A., & Wasserman, I. 2001, *Physical Review D*, 65, 024001, doi: [10.1103/PhysRevD.65.024001](https://doi.org/10.1103/PhysRevD.65.024001)

Seidelmann, P. K., Archinal, B. A., A'hearn, M. F., et al. 2007, *Celestial Mechanics and Dynamical Astronomy*, 98, 155, doi: [10.1007/s10569-007-9072-y](https://doi.org/10.1007/s10569-007-9072-y)

Spilker, L. 2019, *Science*, 364, 1046, doi: [10.1126/science.aat3760](https://doi.org/10.1126/science.aat3760)

Stacey, F. D., & Davis, P. M. 2004, *Physics of the Earth and Planetary Interiors*, 142, 137, doi: [10.1016/j.pepi.2004.02.003](https://doi.org/10.1016/j.pepi.2004.02.003)

Stanley, S. 2010, *Geophys. Res. Lett.*, 37, L05201, doi: [10.1029/2009GL041752](https://doi.org/10.1029/2009GL041752)

Stevenson, D. J. 1982, *EOS Transactions of the American Geophysical Union*, 63, 1020

Stevenson, D. J. 1982, *Geophysical and Astrophysical Fluid Dynamics*, 21, 113, doi: [10.1080/03091928208209008](https://doi.org/10.1080/03091928208209008)

Stevenson, D. J. 2020, *Annual Review of Earth and Planetary Sciences*, 48, 465

Stevenson, D. J., & Salpeter, E. E. 1977, *ApJS*, 35, 239, doi: [10.1086/190479](https://doi.org/10.1086/190479)

Sur, A., Burrows, A., Arevalo, R. T., & Su, Y. 2025a, *ApJ*, 994, 186, doi: [10.3847/1538-4357/ae16a3](https://doi.org/10.3847/1538-4357/ae16a3)

Sur, A., Su, Y., Tejada Arevalo, R., Chen, Y.-X., & Burrows, A. 2024, *ApJ*, 971, 104

Sur, A., Tejada Arevalo, R., Burrows, A., & Chen, Y.-X. 2025b, arXiv e-prints, arXiv:2510.08681, doi: [10.48550/arXiv.2510.08681](https://doi.org/10.48550/arXiv.2510.08681)

Sur, A., Tejada Arevalo, R., Su, Y., & Burrows, A. 2025c, ApJL, 980, L5, doi: [10.3847/2041-8213/adad62](https://doi.org/10.3847/2041-8213/adad62)

Takata, M., & Saio, H. 2013, PASJ, 65, 68, doi: [10.1093/pasj/65.3.68](https://doi.org/10.1093/pasj/65.3.68)

Tejada Arevalo, R. 2025, The Astrophysical Journal Letters, 989, 15, doi: [10.3847/2041-8213/adf3a5](https://doi.org/10.3847/2041-8213/adf3a5)

Tejada Arevalo, R., Su, Y., Sur, A., & Burrows, A. 2024, ApJS, 274, 34, doi: [10.3847/1538-4365/ad6cd7](https://doi.org/10.3847/1538-4365/ad6cd7)

Tejada Arevalo, R., Sur, A., Su, Y., & Burrows, A. 2025, ApJ, 979, 243, doi: [10.3847/1538-4357/ada030](https://doi.org/10.3847/1538-4357/ada030)

Vazan, A., Helled, R., & Guillot, T. 2018, Astronomy & Astrophysics, 610, L14

Wahl, S. M., Hubbard, W. B., Militzer, B., et al. 2017, Geophysical Research Letters, 44, 4649

Wood, T. S., Garaud, P., & Stellmach, S. 2013, The Astrophysical Journal, 768, 157, doi: [10.1088/0004-637X/768/2/157](https://doi.org/10.1088/0004-637X/768/2/157)

Yan, C., & Stanley, S. 2021, AGU Advances, 2, e00318, doi: [10.1029/2020AV000318](https://doi.org/10.1029/2020AV000318)

Zhang, J., & Rogers, L. A. 2022, ApJ, 938, 131, doi: [10.3847/1538-4357/ac8e65](https://doi.org/10.3847/1538-4357/ac8e65)

Zhang, S., Fuentes, J. R., & Cumming, A. 2025, ApJL, 991, L23, doi: [10.3847/2041-8213/ae0459](https://doi.org/10.3847/2041-8213/ae0459)

## APPENDIX

## A. RELEVANCE OF HELIUM RAIN FOR SEISMOLOGY?

Helium rain introduces a helium gradient across the immiscibility region. It has accordingly been suggested that this region may be stably stratified, which may then play a role in the interpretation of Saturn's seismology (e.g., [C. R. Mankovich & J. Fuller 2021](#)). In the course of our work, we found that the rain region generally does not produce stably stratified regions that affect the crucial W76.44 frequency. In this section, we provide an analytical argument for why this is the case.

In the immiscible region, the thermodynamic profile remains marginally convectively unstable throughout. This is because any stable regions cease to efficiently transport helium and energy, resulting in significant accumulation of helium and heat beneath the stable region that quickly overwhelms the stabilizing gradients. Thus, in the absence of semiconvection, the rain region should remain fully convective. This is largely borne out by the results shown here (e.g., Figs. 3). Note that a small Brunt-Väisälä frequency can be seen in the immiscible region. This is because in the operator splitting adopted by **APPLE**, each timestep consists of a thermodynamic adjustment followed by a hydrostatic one. Thus, even though the rain region is fully convective after the thermodynamic adjustment (verified by inspection), it can become marginally convective after the hydrostatic adjustment.

To then understand the circumstances under which stable stratification due to helium rain can arise, some semiconvective transport must be adopted. To qualitatively understand the effect of semiconvective transport, we adopt the  $R_\rho$  prescription ([C. Mankovich et al. 2016](#); [A. Sur et al. 2025a](#)), which we briefly summarize below. Note that our results will qualitatively apply to more physical models of semiconvective transport as well (e.g.,  $R_\rho = 0$  corresponds to highly efficient semiconvection).

In **APPLE**, the  $R_\rho$  prescription is implemented as a modification to the convective velocity ([C. R. Mankovich & J. Fuller 2021](#); [A. Sur et al. 2024, 2025a](#))

$$v_{\text{conv}} \propto \left\{ -\frac{dS}{dr} + \left( \left( \frac{\partial S}{\partial Y} \right)_{PT} (1 - R_\rho) + \left( \frac{\partial S}{\partial Y} \right)_{P\rho} R_\rho \right) \frac{dY}{dr} \right\}_+^{1/2}, \quad (\text{A1})$$

where the + subscript denotes taking the maximum of the bracketed quantity and zero. In the limit  $R_\rho = 1$ , convective energy transport sets in only once the planetary fluid becomes unstable under the Ledoux condition ([P. Ledoux 1947](#)). On the other hand, in the limit  $R_\rho = 0$ , convective energy transport becomes possible as soon as the planetary fluid is unstable under the Schwarzschild condition (see [A. Sur et al. 2025a](#) for a more detailed discussion), modeling efficient energy transport via semiconvective processes such as double diffusive instabilities (e.g. [J. Leconte & G. Chabrier 2012, 2013](#); [P. Garaud 2018](#)). We explicitly remark that the physical convective stability of the fluid, used to calculate the Brunt-Väisälä frequency, is always evaluated using the Ledoux condition regardless of the value of  $R_\rho$  adopted.

A nonzero  $N$  in the helium rain region appears when  $R_\rho < 1$  is taken, since the effective convective flux ( $\propto v_{\text{conv}}^3$ ) can be nonzero even when the fluid is physically convectively stable. In our numerical experiments, the stably stratified regions due to helium rain were unable to support large  $g$  mode frequencies, and we provide a qualitative justification for this here. Recall that standard expressions for the  $g$  mode frequencies typically scale as

$$\omega_g^2 \simeq \frac{N^2 l(l+1)}{r^2 k_r^2}, \quad (\text{A2})$$

where  $r$  is the radius of the stably stratified cavity and  $k_r$  is the mode radial wavenumber. The largest frequencies then correspond to the smallest  $k_r$ , or the largest wavelength. For a cavity with radial extent  $\delta r$  (set by the extent of the immiscible region),  $k_{r,\text{max}} \simeq 2\pi/(\delta r)$ . Then,  $N^2$  also depends on  $\delta r$  via the maximum extent of compositional stratification possible in the rain region. By expanding  $N^2$  in terms of structural and thermodynamic derivatives, we find that

$$\omega_g^2 \simeq \frac{l(l+1)}{4\pi^2} \left( \frac{\delta r}{r} \right)^2 \times \left[ -\frac{g}{\rho} \left( \frac{\partial \rho}{\partial S} \right)_{PY} \left( \frac{dS}{dr} - \left( \frac{\partial S}{\partial Y} \right)_{P\rho} \frac{dY}{dr} \right) \right]. \quad (\text{A3})$$

But then, since the fluid satisfies marginal instability, some light algebra shows that

$$0 \approx \frac{dS}{dr} - \left[ \left( \frac{\partial S}{\partial Y} \right)_{PT} (1 - R_\rho) + \left( \frac{\partial S}{\partial Y} \right)_{P\rho} R_\rho \right] \frac{dY}{dr}, \quad (\text{A4})$$

$$\frac{\omega_g^2}{\Omega_{\text{dyn}}^2} \simeq \left\{ \frac{g}{g_{\text{surf}}} \left( \frac{\partial \ln \rho}{\partial S} \right)_{PY} \left[ \left( \frac{\partial S}{\partial Y} \right)_{PT} - \left( \frac{\partial S}{\partial Y} \right)_{P\rho} \right] \right\} (1 - R_\rho) \frac{l(l+1)}{4\pi^2} \left( \frac{R \delta r}{r^2} \right) \Delta Y, \quad (\text{A5})$$

Here,  $g$  denotes the local gravitational acceleration, and  $g_{\text{surf}}$  that at Saturn's surface. The quantity in the curly braces is typically of order unity (0.5–1) throughout the planet. Thus, for an  $\ell = 2$  mode, the typical mode frequencies expected scale like  $\sim \sqrt{(1 - R_\rho) \Delta Y R(\delta r) / r^2}$ . As can be seen, this number generally remains below 1, and does not reach  $\sim 2$  as would be required to be relevant to the W76.44 oscillation frequency.